remote sensing

MDPI

Communication

Injection of High Chlorophyll-a Waters by a Branch of Kuroshio Current into the Nutrient-Poor North Pacific Subtropical Gyre

Chun-Hoe Chow [1,*], Yi-Chen Lin [1], Wee Cheah [2] and Jen-Hua Tai [3]

[1] Department of Marine Environmental Informatics, National Taiwan Ocean University, Keelung 202301, Taiwan; 00781056@email.ntou.edu.tw
[2] Institute of Ocean and Earth Sciences, Universiti Malaya, Kuala Lumpur 50603, Malaysia; wee.cheah@um.edu.my
[3] Research Center for Environmental Changes, Academia Sinica, Taipei 115, Taiwan; jhtai@gate.sinica.edu.tw
* Correspondence: kilmerchow@email.ntou.edu.tw

Abstract: An unusual eastward flow was observed branching out from the Kuroshio Current near the island of Taiwan in the western North Pacific in during the period June–July 2010. The branch meandered eastward approximately 21°N, carrying high chlorophyll-a (Chla) waters for over 1000 km from 125°E into the nutrient-poor North Pacific subtropical gyre (NPSG). The branch was warmer and fresher than the surrounding waters, with temperature–salinity properties resembling those of Kuroshio Current. Thus, we called it the eastward cross-shore Kuroshio branch (ECKB). Injecting fresher waters far into the central NPSG, the ECKB flowed at a mean surface speed of 0.5 m per second, as shown in satellite altimeters, a Lagrangian drifter, and the Japan-Meteorological-Agency (JMA) 137°E-meridian cruise transect. The mechanism of the ECKB was linked to a surface cyclonic wind anomaly to the north at approximately 22–24°N. The cyclonic wind anomaly cooled the ocean surface beneath it via Ekman suction and then enhanced the subtropical front to its south at approximately 21°N near the Kuroshio Current. The strengthened subtropical front subsequently induced an eastward flow that bifurcated from the main stream of the northward-flowing Kuroshio Current.

Keywords: Kuroshio branch; salinity; chlorophyll-a; North Pacific subtropical gyre; satellite observation; in situ observation

Citation: Chow, C.-H.; Lin, Y.-C.; Cheah, W.; Tai, J.-H. Injection of High Chlorophyll-a Waters by a Branch of Kuroshio Current into the Nutrient-Poor North Pacific Subtropical Gyre. *Remote Sens.* **2022**, *14*, 1531. https://doi.org/10.3390/rs14071531

Academic Editor: Emmanuel Devred

Received: 18 February 2022
Accepted: 20 March 2022
Published: 22 March 2022

1. Introduction

In the subtropical North Pacific, surface ocean circulation is dominated by a wind-driven, clockwise-circulating North Pacific Subtropical Gyre (NPSG). At the western boundary of the NPSG, a fast-flowing western boundary current called the Kuroshio Current (KC) [1] connects the North Pacific Current in the north and the North Equatorial Current (NEC) in the south near the equator (Figure 1a). The KC, meaning "black stream" in Japanese, obtained its name due to the black color or precisely the deep blue color of its waters. The deep blue color of the KC is mostly due to a lack of phytoplankton as a result of nutrient depletion especially in waters off the east of Taiwan [2].

Against the westward-flowing NEC, a slow surface countercurrent flows eastward at speeds of approximately 2–10 cm s^{-1} [3–5]. This slow current is the North Pacific Subtropical Countercurrent (STCC) (Figure 1a), which was first reported by Uda and Hasunuma [6] from in situ observations. The STCC is strong in late winter to spring (March–June) with a peak in June, however, it is weak in fall [7]. The STCC is much slower than the KC, and its footprint cannot be clearly observed in the climatology geostrophic flow in July (Figure 1b). Between the main stream of the northward-flowing KC and the eastward-flowing STCC, the Kuroshio recirculation (KR; Figure 1a) generally occurs east of the Taiwan Island during the interaction between the KC and the mesoscale eddies that propagate from the east [4,8–12]. Based on computer simulations, Chu et al. [4] concluded that the STCC originates from the east of the Luzon Strait at approximately 122.5°E on the

23.5-sigma isopycnal surface. The STCC generally emerges from the southeastward turning of the KR, which centers at approximately 124°E and 24°N [4].

The mechanism for the changes of the STCC has been linked to changes in the surface [5,13] and subsurface (below the mixed layer) [7] subtropical fronts. Over long-term time scales (mean state and a decadal time scale from 1965 to 2008), the STCC was anchored and maintained by the subtropical mode water (STMW) [14–17], whereas for shorter timescales (seasonal and interannual), the STCC strength was suggested to be determined by the subtropical fronts, which were influenced by surface wind forcing rather than the surface thermal condition [5,7,18]. In addition, a recent study by Zhang and Xue [19] indicated that the width of the Luzon Strait might also play a key role in the formation of the STCC.

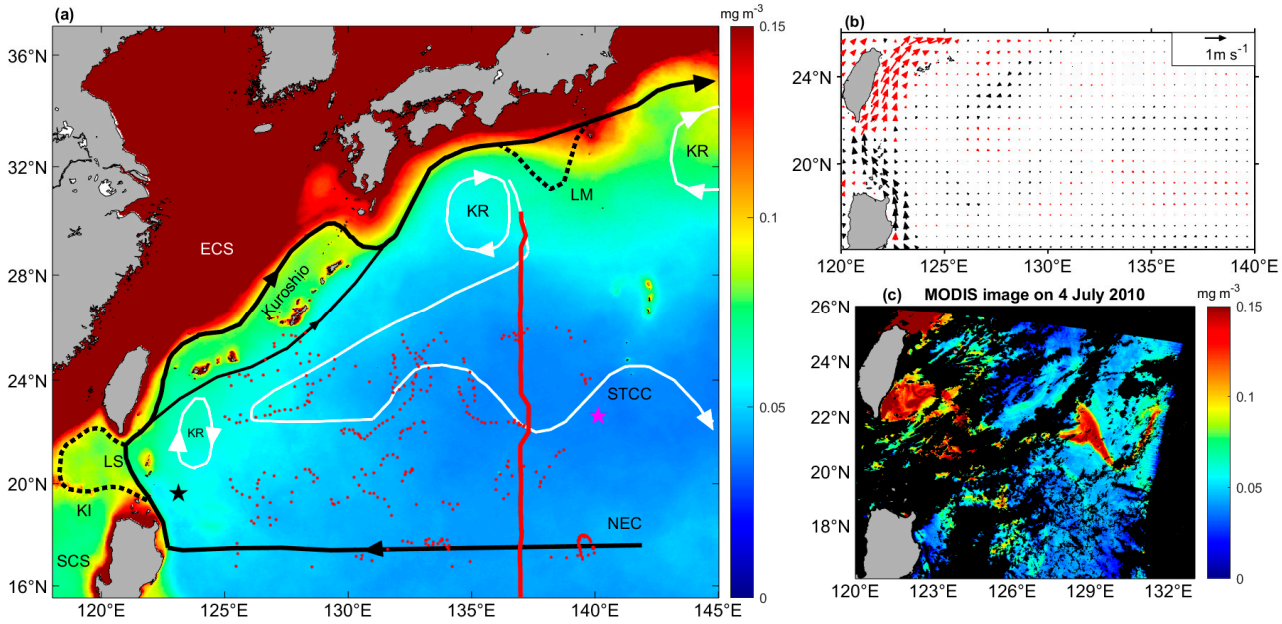

Figure 1. (**a**) Schematic of the Kuroshio Current (KC) circulation system [1,8,20] superimposed on the climatology 1/24°-gridded chlorophyll-a (Chl-a; color shaded) in July from 1998 to 2020. The black bold solid line with arrows shows the flow of the KC and its connection with the North Equatorial Current (NEC). The white circles show the clockwise Kuroshio recirculation (KR) near Japan [1] and Taiwan [8]. The white wave-pattern curve near 22°N indicates the eastward-flowing Subtropical Countercurrent (STCC) [6]. The black dashed curves show the large meandering (LM) of KC south of Japan [1] and the loop of Kuroshio intrusion (KI) via the Luzon Strait (LS) into the South China Sea (SCS) [21]. The meridional red bold line denotes the 137°E transect. The red dots show the locations of the Argo profiles used in this study. Black and magenta stars show the locations of background water masses near the KC and the STCC, respectively; (**b**) climatology of 1/4°-gridded geostrophic flow in July from 1998 to 2020 with red arrows indicating positive zonal velocities and black arrows indicating negative zonal velocities; (**c**) Aqua-MODIS Level 2 Chl-a image at 1 km spatial resolution taken on 4 July 2010.

Near the Luzon Strait, the KC typically bifurcates with one branch to the west (Figure 1a), intruding into the South China Sea (SCS) [21] during persistent northeasterlies in boreal winter. With the KC intruding into the SCS, the KR can be induced east of the Luzon Strait (Figure 1a) centering at approximately 123°E–124°E and 21°N–22°N [7], which is a region with many active anticyclonic eddies [22]. In contrast, without the Kuroshio intrusion (KI) in summer, the KR can be caused by the impinging of an anticyclonic eddy with the KC eastern flank [8].

In this study, we reported a filament of high chlorophyll-a (Chl-a) (>0.07 mg m^{-3}) which occurred in the active area of KR [8] and anticyclonic eddies [22] in July 2010, which can be observed via the Level 2 satellite image taken from the Moderate Resolution Imaging

Spectroradiometer (MODIS) sensor onboard the Aqua satellite (Figure 1b) and in daily images of the merged satellite ocean color product (Figure 2). Based on a suite of satellite and in situ observations, we found that the high Chl-a filament delineated the footprint of an unusual eastward flow (compared to the July climatology field in Figure 1b) branching out from the KC. This study designated the unusual eastward flow as the eastward cross-shore Kuroshio branch (ECKB) which could be observed in other years. In this study, we solely focused on the potential mechanisms that contribute to the 2010 ECKB and its impact on the oligotrophic NPSG.

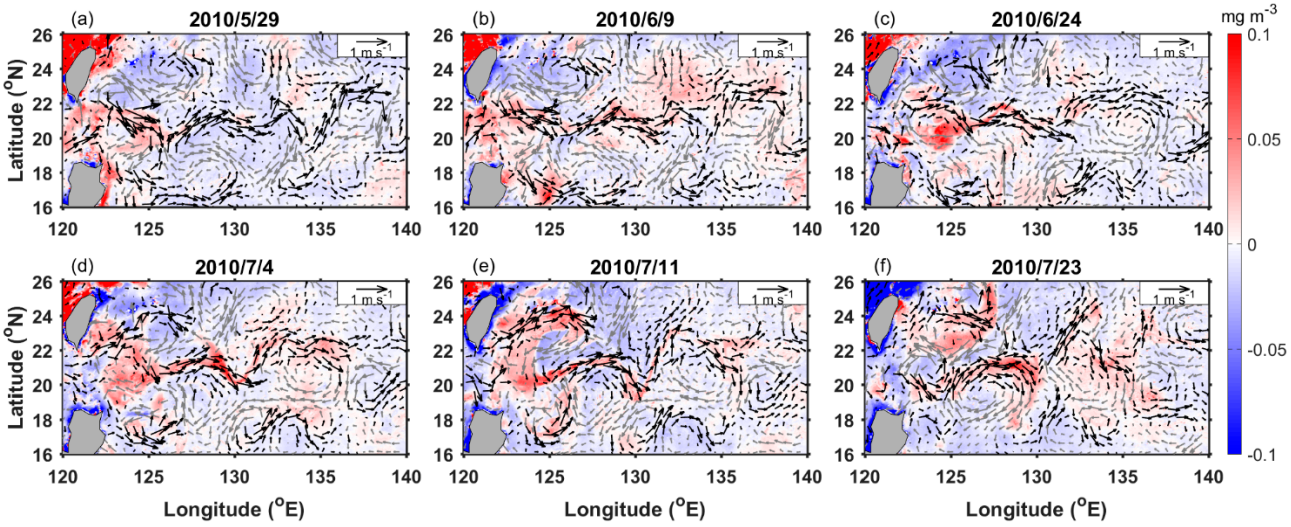

Figure 2. The filament evolution shown as daily 1/24°-gridded chlorophyll-a (Chl-a) anomalies (color shaded) for the selected days (**a**) 29 May, (**b**) 7 June, (**c**) 24 June, (**d**) 4 July, (**e**) 11 July and (**f**) 23 July 2010, in references to the 23 years (1998–2020) daily Chl-a climatological mean. The arrows show the geostrophic velocity anomalies (black for positive zonal velocities and gray for negative zonal velocities) based on the altimetry 1/4°-gridded product. The high Chl-a anomalies located along 21°N within 125°E and 135°E show the footprint of the eastward cross-shore Kuroshio branch (ECKB).

2. Data and Methods

As cloud-cover is a major issue in the study region, especially in summer (June and July), we used the daily Level 4 or "cloud-free" (interpolated) Copernicus-GlobColour Chl-a data, available since 1997, at 1/24° spatial resolution (https://doi.org/10.48670/moi-00100, accessed on 12 August 2020). The Chl-a data were produced by merging Chl-a from multiple ocean color sensors namely the Sea-Viewing Wide Field-of-View Sensor (SeaWiFS), MODIS, Medium Resolution Imaging Spectrometer (MERIS), Visible Infrared Imaging Radiometer Suite (VIIRS), and Ocean and Land Colour Instrument (OLCI). The "cloud-free" Chl-a data were calculated based on a combination of algorithms for different water types (oligotrophic, Chl-a dominated, and coastal turbid) and an optimal interpolation using the kriging method with regional anisotropic covariance models [23]. To ensure that the Level 4 Copernicus-GlobColour Chl-a was capturing real ocean color signals and not artifacts from interpolation, we cross-checked the Level 4 data with Level 2 Chl-a data (as shown in Figure 1c) obtained from NASA's Oceancolor Web (https://doi.org/10.5067/AQUA/MODIS/L2/OC/2018, accessed on 3 February 2022).

We used the altimeter ADT data at 1/4° spatial resolution from the Global Ocean Gridded Level 4 Sea Surface Heights and Derived Variables Reprocessed product (https://doi.org/10.48670/moi-00148, accessed on 9 July 2019), which provides the absolute geostrophic velocities and geostrophic velocity anomalies. The SST data were obtained from the OSTIA [24] global SST reprocessed product (https://doi.org/10.48670/moi-00168, accessed on 18 December 2021) that provides gap-free maps of foundation SST and ice

concentration at 0.05° spatial resolution, based on satellite and in situ data. For winds, we used the monthly Cross-Calibrated Multi-Platform (CCMP) gridded 10 m winds available from July 1987 to April 2019, based on satellite, moored buoy, and model data, made available at 1/4° spatial resolution by the Remote Sensing Systems (RSS) at www.remss.com (accessed on 1 October 2020).

For in situ observations, we used data obtained from a Lagrangian surface drifter, Argo floats, and scientific cruises. These in situ observations were selected based on their locations that were along/near to the Chl-a filament from May to July 2010. The Argo ocean vertical profiles and the drifter-trajectory data were collected and made available by the Coriolis project and programs that contribute to the French operational oceanography program for in situ observations (http://www.coriolis.eu.org, accessed on 21 May 2020). Drifter and Argo floats were identified with their World Meteorological Organisation (WMO) numbers. The particular drifter and Argo floats were called with their WMO number hereafter. We only used those data of temperature and salinity with good-flagged quality from 361 Argo profiles (their locations are shown in Figure 1a). The surface current data of the drifter were used from May to June 2010 (only available until 24 June 2010), to compare with the satellite observations.

Additional in situ temperature and salinity profiles were obtained from the CTD casts measured by the Japan Meteorological Agency (JMA) along the 137°E meridional cruise transect (hereafter referred to as the 137°E transect), which was across the Chl-a filament during the period 14–16 July 2010. The JMA repeatedly carried out oceanographic and marine meteorological observations through research vessels in the western North Pacific. The data can be obtained from the web pages at https://www.data.jma.go.jp/gmd/kaiyou/db/vessel_obs/data-report/html/index_e.html (accessed on 25 November 2016) [25].

We used historical ocean profiles along and around the ECKB, obtained via Argo floats and the 137°E transect (Figure 1a), to observe the relative changes in water-mass properties. The observed ocean profiles were compared to the climatological field in the region of KC and NPSG (black and purple stars, respectively, in Figure 1a). In addition, observations from three Argo floats along the high Chl-a filament were used to detect fresher waters transported by the ECKB. From west to east along the ECKB, the WMO numbers of these three Argo floats were WMO 5901521, 5901512, and 2901588. The drifter WMO 22527 was carried along the ECKB from May to June 2010.

To study the wind forcing that drives the ECKB, we estimated the surface wind stress $(\overline{\tau_x}, \overline{\tau_y})$ using:

$$\overline{\tau}_x = \rho_a \times C_d \times spd_w \times u_w \tag{1}$$

$$\overline{\tau}_y = \rho_a \times C_d \times spd_w \times v_w \tag{2}$$

$$10^3 C_d = \frac{2.7}{spd_w} + 0.142 + 0.0764 \times spd_w \tag{3}$$

where the air density $\rho_a = 1.2$ kg m^{-3}, spd_w is the wind speed, u_w is the zonal wind velocity, v_w is the meridional wind velocity, and C_d is the drag coefficient that was computed by following Large and Pond [26]. Then, we followed the work by Qiu and Chen [5] to calculate the meridional Ekman velocity (v_{Ek}) averaged in the surface layer using $v_{Ek} = -\tau_x/(\rho_0 f H_0)$ where ρ_0 is the reference density, f is the Coriolis parameter, and H_0 (=150 m, by following [5]) is the thickness of the surface STCC layer, where the changes of STCC flow are largely confined [5]. Furthermore, we studied the ocean profiles obtained from the CTD casts by calculating the potential vorticity (PV) by ignoring the relative vorticity using:

$$\mathrm{PV} = \frac{f}{\rho_0}\frac{\partial \rho}{\partial z} \tag{4}$$

where ρ is the ocean potential density, z is the depth (positive downward), ρ_0 is the mean ocean potential density between each depth, and f is the Coriolis parameter.

3. Results

3.1. Advection of Chl-a by Ocean Flow along 21°N

Figure 2 shows the selected daily anomalies of Chl-a referring to the daily climatology from 1998 to 2020. The Chl-a filament meandered at approximately 21°N and extended zonally by approximately 1100 km within 125°E and 135°E from 29 May to 23 July 2010. The daily anomalies of Chl-a concentrations are two times higher than the daily climatological mean along the Chl-a filament, displaying how large the anomalies of Chl-a concentration along the filament. To show Chl-a advection by ocean currents, Figure 2 also shows the geostrophic velocity anomalies during the same periods. The altimetry-obtained geostrophic flow matched with the high Chl-a filament, suggesting the Chl-a advection by the eastward-flowing ECKB, which can be seen along 21°N from every daily map shown in Figure 2.

On a monthly timescale, Figure 3 shows the monthly pattern of the Chl-a filament in June and July 2010. The meandering elongation of the Chl-a filament can still be clearly observed in the monthly averaged Chl-a distribution. In Figure 3a, the Chl-a filament starts from an anticyclonic eddy with a high Chl-a around the eddy edge [9] east of the Luzon Strait, matching the surface geostrophic flow obtained from the satellite and drifter observations in June. In Figure 3b, high Chl-a can be observed within the eastward-flowing ECKB, approximately within 125°E and 135°E in July. Note that these monthly patterns of high Chl-a filament and geostrophic flow are rarely observed east of the Luzon Strait in the July climatological field (Figure 1a,b).

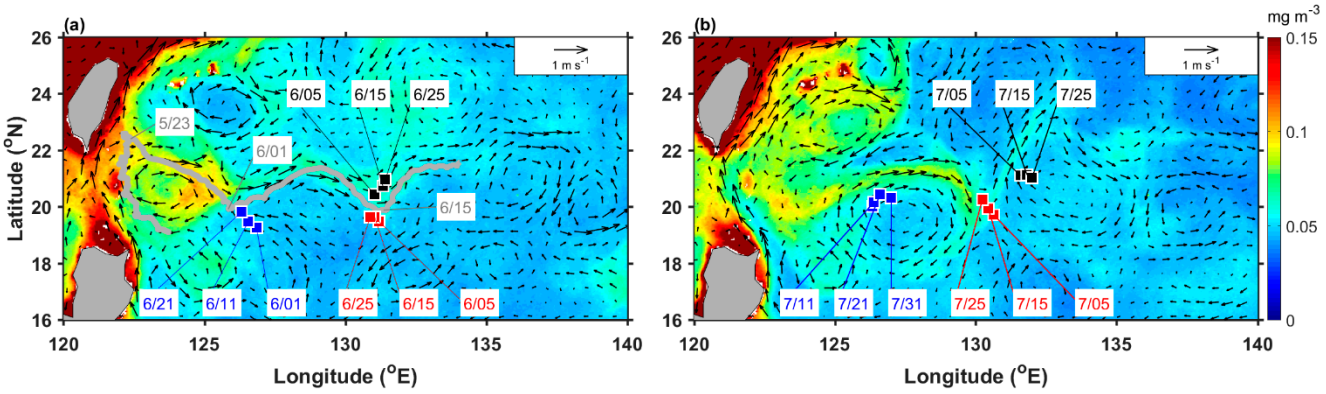

Figure 3. The monthly maps of 1/24°-gridded chlorophyll-a (Chl-a) concentrations (color shaded) and 1/4°-gridded absolute geostrophic velocities (arrows) in (**a**) June and (**b**) July 2010. The square symbols in blue, red, and black show the locations of Argo 5901521, 5901512, and 2901588, respectively, from west to east roughly along the high Chl-a filament. The gray curve in (**a**) shows the trajectory of drifter 22527 in May and June. The high Chl-a filament located along 21°N within 125°E and 135°E shows the footprint of the eastward cross-shore Kuroshio branch (ECKB). The dates (month/days) given in same colors point to the corresponding locations of the drifter and Argo floats.

In Figure 4, the eastward-flowing ECKB is represented by the trajectory of the drifter. The near-surface drifter flowed along the west–east band with large meridional gradients of ADT (Figure 4), where the eastward geostrophic flow was strong (Figure 3) at approximately 21°N. The consistency of altimetry and drifter observations show that the ocean currents along the high Chl-a filament were mainly determined by the geostrophic flow. The drifter moved northward between the KC and an anticyclonic eddy or KR in the east at the beginning of May (Figure 4a). Then, it turned southeastward when approaching 22°N, circling an anticyclonic eddy that was centered at approximately 123.4°E and 20.4°N until the end of May (Figure 4a). In June, the drifter moved further eastward, flowing along the curvature pattern of ADT contours (Figure 4b). Based on the drifter trajectory from May to June, the drifter was carried by the ECKB, which was the Kuroshio bifurcation to the east at approximately 22°N (Figure 4c).

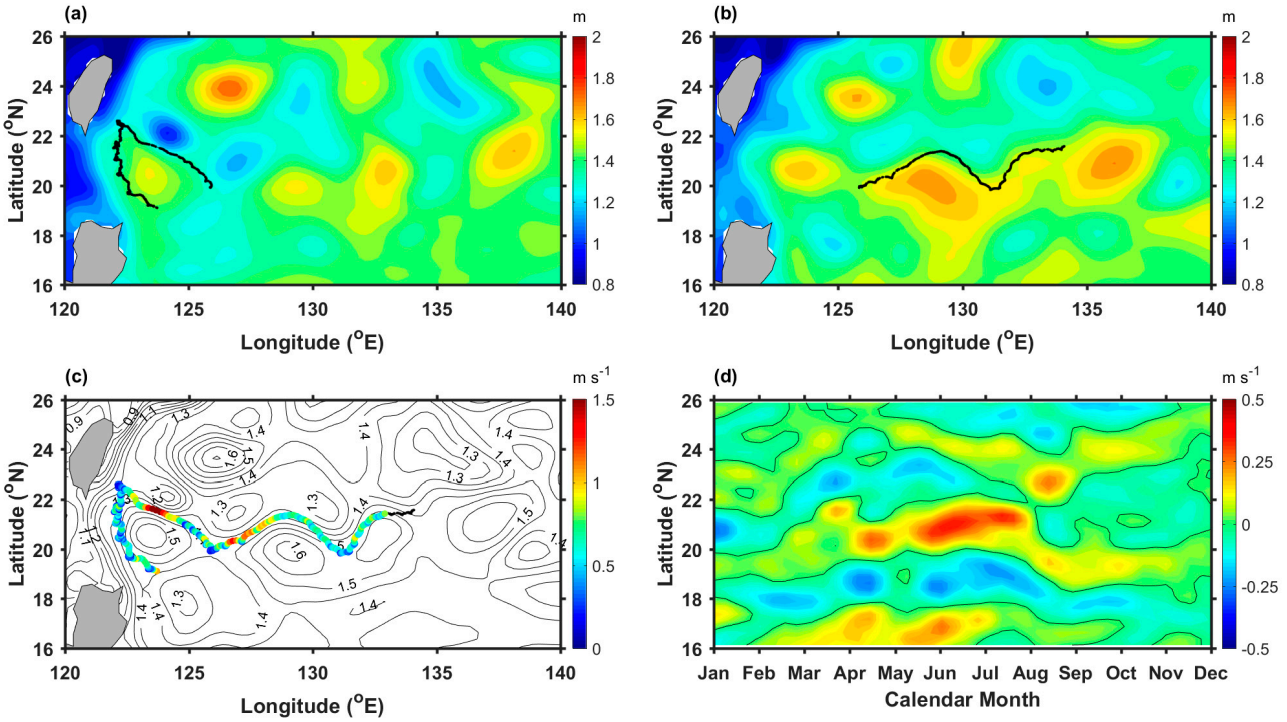

Figure 4. Spatial distribution of satellite-obtained absolute dynamic topography (ADT) averaged in (**a**) May, (**b**) June, and (**c**) from May to June (contours, units in m), in 2010, based on the altimetry 1/4°-gridded product. The black curve in (**a**,**b**) shows the trajectory of drifter 22527 in the relative month. The colored curve in (**c**) shows the drifter-measured current speed along the trajectory. (**d**) Hovmöller diagram of zonal geostrophic-current velocity averaged within 125° and 135°E, with the zero values of zonal geostrophic velocity shown by the thin contours.

The drifter speed can exceed 1 m s^{-1} along the ECKB (Figure 4c). Averaged within 125° and 135°E based on the satellite observation, the ECKB has a zonal speed reaching 0.5 m s^{-1}, which was close to the drifter speed at approximately 0.6 m s^{-1} averaged in the same region. According to the Hovmöller diagram of zonal geostrophic-current velocity shown in Figure 4d, the ECKB began in April, peaked in June and became weaker at the end of July, within 20°N and 22°N. Such a strong eastward flow can transport waters from the western boundary into the high-salinity NPSG where ocean currents are generally weak [27]. Moreover, the seasonal variability of the ECKB in 2010 was found to be similar to that of STCC, which is strong from late winter to spring (March–June), and weak in fall [7].

3.2. Injection of Fresher Waters by Ocean Flow along 21°N into the High-Salinity NPSG

A recent study by Yan et al. [28] showed that waters were getting fresher near the Luzon Strait in the NPSG. The horizontal advection of low-salinity anomalies associated with the KC system was found to be the main mechanism of the observed freshening.

From the time series of salinity and temperature profiles obtained from the three Argo floats along the ECKB from May to July (Figure 5a–c), fresher waters with low salinity below 34.6 ppt can be found above the mixed-layer depth (MLD) at approximately 50 m. Figure 5a–c show the minimum salinity near the surface detected in June and July via the Argo floats, implying fresher waters being transported further to the east of 130°E into the high-salinity region of NPSG, by the ECKB. Moreover, Figure 5a–c show that the MLDs were shallower than 50 m (reaching 25 m) and no MLD deepening could be found via the Argo floats along the Chl-a filament. Thus, this MLD analysis suggests that the Chl-a filament was mainly the result of advection by the ECKB, instead of local upwelling.

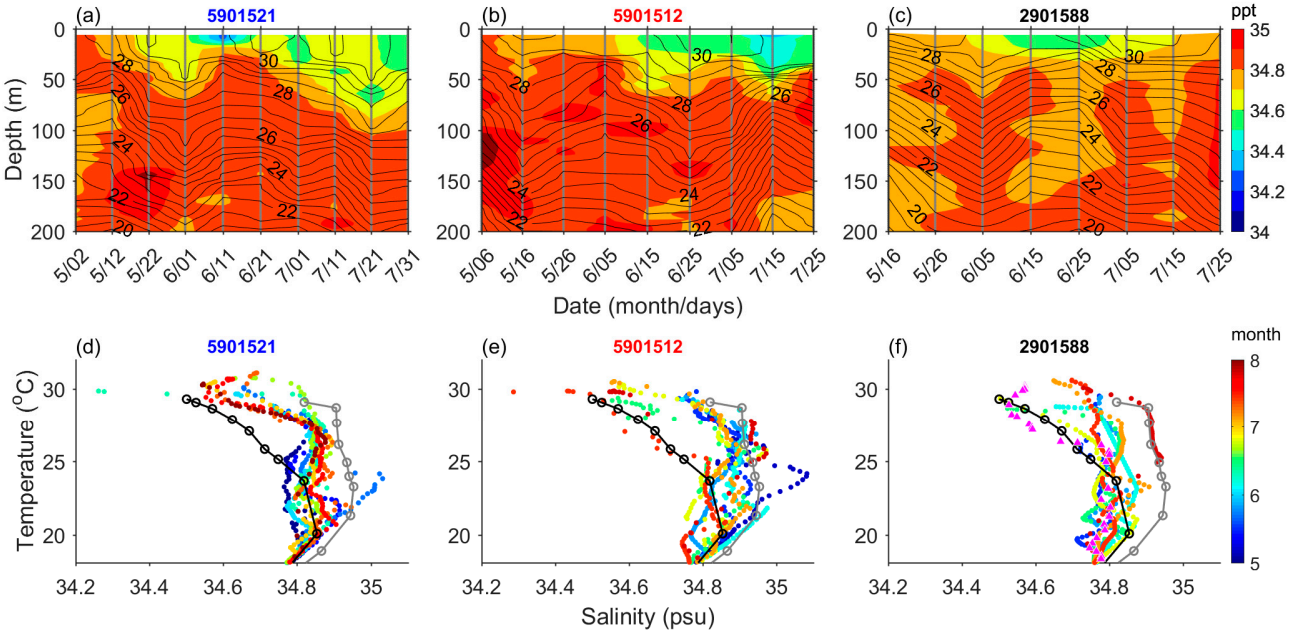

Figure 5. (**a**–**c**) Time series of salinity (color shaded) and temperature (contours) profiles corresponding to three selected Argo floats with the WMO numbers of 5901521, 5901512, and 2901588, from May to July 2010. The locations of these three Argo floats are marked in Figure 3. (**d**–**f**) Temperature–salinity (TS) diagrams corresponding to the profiles of three selected Argo floats shown in (**a**–**c**), respectively. Colors show the time in the calendar month. The magenta triangles in (**f**) show the TS properties obtained from the CTD casts near 137°E and 23°N in July 2010. Black and gray curves with circles show the background TS properties averaged in June and July, located at the black and magenta star, respectively, shown in Figure 1a. Note: Not all data points are shown in the figures for better clarity, but the scientific results are not affected by the unshown data points.

According to the temperature–salinity (TS) diagrams shown in Figure 5d–f, the Kuroshio water masses, which are fresher than those in the NPSG, can be detected along the ECKB. In Figure 5d, waters with salinity lower than 34.5 ppt could be found via the profiles of Argo 5901251 near 126°E (Figure 3a) during mid-June. In Figure 5e, low salinity waters could also be found to the east via the profiles of Argo 5901512 near 130°E (Figure 3b) during mid-July. The TS diagrams with lower salinity were similar to that of the KC background (see the black star in Figure 1a for the location) displayed by the black circled curves within 20–30 °C in Figure 5e,f, observed by Argo 5901512 and Argo 2901588 in July and June, respectively. Moreover, the fresher Kuroshio waters could be detected further to the east at 137°E (Figure 5f), as observed from the CTD measurements near 23°N along the 137°E transect. These TS properties show that the fresher Kuroshio waters were detected along the Chl-a filament, suggesting the injection of fresh and high-Chl-a-concentration waters by the ECKB into the high-salinity and nutrient-poor NPSG.

In Figure 6a,b, the ECKB was warmer and fresher above 50 m near 23°N than its surroundings, based on the CTD profiles along the 137°E transect. The temperature vertical structures concaved downward at the main axis of the ECKB, separating colder, denser waters north of 26°N and warmer, lighter waters south of 20°N (Figure 6a,c) above 200 m. In Figure 6c, the ECKB can be seen above the southern boundary of low PV waters, which might be the STMW [4] where its boundary is defined by the PV value at 2.5×10^{-10} s^{-2} [29]. The zonal geostrophic speed of the ECKB reached 0.5 m s^{-1} at the surface (Figure 6d), by assuming zero velocity at 1000 m. This zonal geostrophic speed estimated from the CTD casts was consistent with that obtained from the drifter and satellite observations west of 135°E.

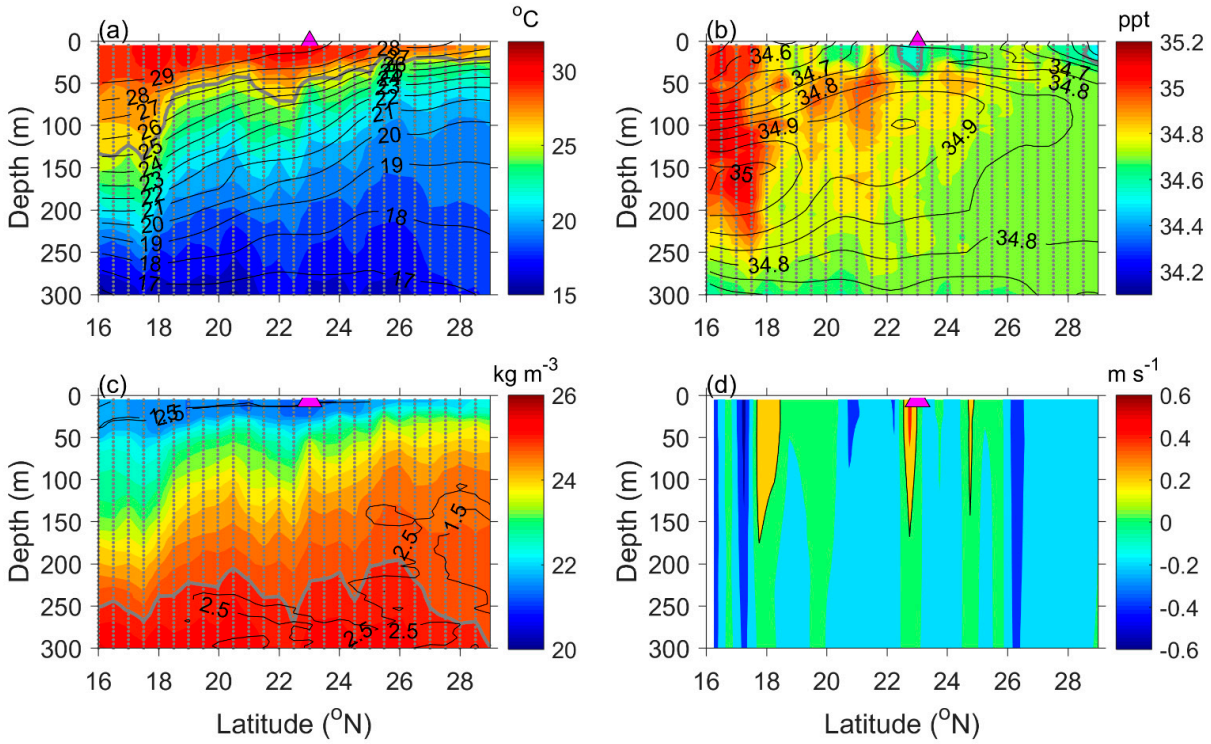

Figure 6. Profiles of (**a**) temperature, (**b**) salinity, (**c**) potential density, and (**d**) zonal geostrophic velocity, measured along the 137°E transect in July 2010. In (**a**–**c**), bold gray contours show the contour of temperature and salinity at 26 °C, 34.6 ppt, and 25 kg m^{-3}, respectively. Black thin contours show the July climatological field in (**a**,**b**), low potential vorticity at 1.5 × 10^{-10} s^{-2} and 2.5 × 10^{-10} s^{-2} in (**c**), and zonal geostrophic velocity at 0.2 m s^{-1} in (**d**). The purple triangles near the surface at approximately 23°N in all figures indicate the location of the CTD station, which corresponds to the purple triangles in the temperature-salinity diagram shown in Figure 5f. Gray dots in (**a**–**c**) show the location of CTD stations and depth resolution.

Warmer temperature (Figure 6a) and zonal geostrophic velocities (Figure 6d) near 23°N show the ECKB depth approaching 200 m. The main axis of the ECKB was approximately located at 23°N with a meridional width of approximately 50 km. The ECKB axis observed via the CTD measurements (Figure 6) matched the location of the high Chl-a filament and fast eastward geostrophic flow (Figures 2 and 3). The consistency of the ECKB information from different observations shows the existence of ECKB, which has not been previously reported. Figure 7 further shows the surface warming around the region of the high Chl-a filament in July 2010 (compared to the July climatology field from 1998 to 2020), and the daily coincidence of surface warming (>30 °C) with the high Chl-a filament on 12 July 2010. No signature of colder water upwelled from below could be observed in the upper mixed layer down to ~50 m (Figure 5a–c), suggesting that local upwelling in the ocean-front region is not the main mechanism causing the high Chl-a filament.

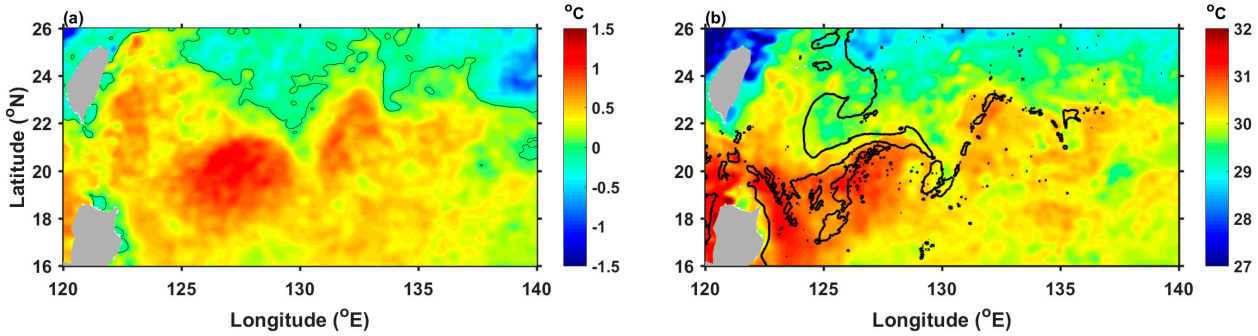

Figure 7. Spatial distribution of (**a**) monthly SST anomalies in July 2010 referring to the month climatology from 1998 to 2020, and (**b**) daily SST on 12 July 2010, based on the OISST product gridded at 0.05°. Thin curve in (**a**) show the zero contour of SST anomalies. Bold curve in (**b**) shows the Chl-a contour at 0.07 mg m^{-3}, representing the high Chl-a filament.

3.3. Mechanisms Driving the ECKB

In Figure 6a, the tilting of background isotherms can be observed at the subsurface below 50 m along the 137°E transect. The eastward flow would be induced under such conditions with isotherm tilting upward to the north, according to the thermal wind balance:

$$f\frac{\partial U_g}{\partial z} = -\alpha g\frac{\partial T}{\partial y} \tag{5}$$

where T is the ocean temperature, g is the gravity, and α is the thermal expansion coefficient. A negative value of $\partial T/\partial y$ indicates an enhanced isotherm tilting. Thus, the stronger the subtropical front (larger $\left|\frac{\partial T}{\partial y}\right|$), the faster the eastward flow near the surface is. The isotherm tilting is related to the subtropical front that was accompanied by colder waters in the north and warmer waters in the south.

Figure 8 shows the TS properties of different water masses separated by the subtropical front as observed via all available good-quality Argo floats in the research area from May to July 2010. Waters north of the front were fresher (Figure 8) than those in the south in May and June 2010. This comparison shows that the subtropical front was formed between two different water masses, which might be converged by the Ekman transport from the north and the south.

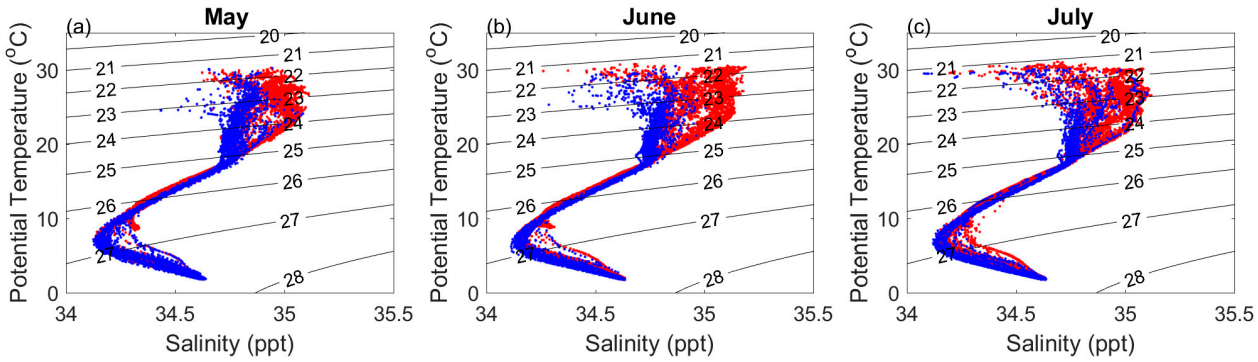

Figure 8. Temperature–salinity (TS) diagrams in (**a**) May, (**b**) June, and (**c**) July, obtained from the Argo floats with their locations shown in Figure 1b. Blue and red dots show the TS properties corresponding to the absolute dynamic topography (ADT) smaller and larger than 1.45 m (north and south of subtropical front), respectively. Black contours show the potential density.

Based on the satellite observations, the subtropical front variation could be observed in the spatial distribution of SST and meridional SST gradients (Figure 9) from May to July 2010. Figure 9a,b show large meridional SST gradients (negative signs) along the ECKB

within 125°E and 135°E from May to June, representing the subtropical front. However, meridional SST gradients became smaller, and the SST distribution was more homogeneous in July than in the previous months (Figure 9c), showing the weakening of the subtropical front.

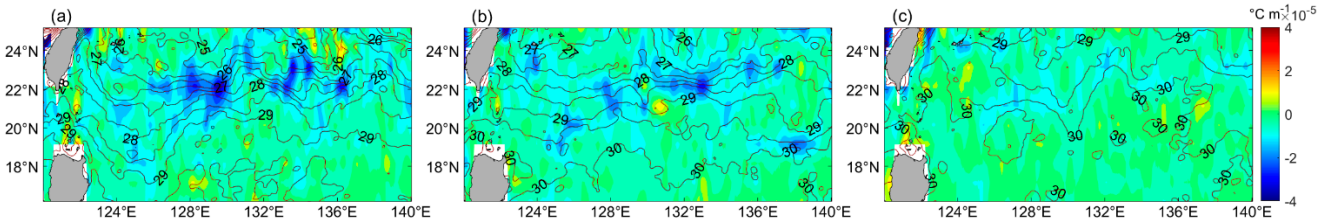

Figure 9. Spatial distribution of meridional SST gradient (color shaded) and SST (contours, units in °C) during (**a**) May, (**b**) June, and (**c**) July 2010, based on the OISST product gridded at 0.05°.

Overall, the subtropical front was represented by large meridional SST gradients that tilt slightly at a southwest–northeast orientation within 20°N and 25°N, consistent with the northernmost subtropical front reported by Kobashi et al. [15], who focused on the long-term mean of three subtropical fronts in the NPSG. Large meridional SST gradients could also be observed near the KC east of the Luzon Strait in May and June (Figure 9a,b), which have rarely been reported in previous studies. This implies that the elongation of the subtropical front can reach the western boundary in the North Pacific on time scales shorter than a season.

Qiu and Chen [5] found that meridional Ekman convergence ($\partial v_{Ek}/\partial y < 0$) mainly contributed to the strengthening of the subtropical front that enhanced the eastward-flowing STCC to produce more eddies via baroclinic instability on interannual time scales, according to the Ekman convergence, forcing:

$$\frac{\partial G}{\partial t} \approx -\frac{\partial}{\partial y}(v_{Ek}G) \tag{6}$$

where G is defined as meridional SST gradients ($-\partial T/\partial y$) and v_{Ek} is the meridional Ekman velocity. However, Kobashi and Xie [7] found that the Ekman suction enhanced by the strong cyclonic wind anomaly elevates the thermocline, decreases SST, and then induces the SST front, accelerating the STCC from late winter to spring (March–June) on interannual time scales.

To confirm the mechanisms enhancing the subtropical front near the KC, we estimated the $-\partial(v_{Ek}G)/\partial y$ term [5] and wind stress curl anomaly [7], averaged within 125–135°E and 20–23°N, from May to July 2010. Figure 10 shows the latitude–time changes of the relative forcing on the subtropical front. Positive wind stress curl and positive wind–stress–curl anomalies were formed north of 21°N from April to June 2010 (Figure 10a,b). The Ekman suction and divergence ($\partial v_{Ek}/\partial y > 0$) would occur beneath the cyclonic wind stress within 21–24°N according to the Ekman theory. Then, SST decreased and the SST anomalies reached −1 °C (Figure 10d) below the cyclonic wind stress anomaly, enhancing the subtropical front (Figure 10c) in the south and thus accelerating the ECKB via thermal wind balance [7]. On the other hand, the $-\partial(v_{Ek}G)/\partial y$ term has negative values ranging from -0.2×10^{-14} to -2×10^{-14} °C m^{-1} s^{-1} from May to June 2010, averaged within 125–135°E and 20–24°N (the area with negative meridional SST gradients, i.e., strong SST front). The negative $-\partial(v_{Ek}G)/\partial y$ term shows that the enhancing of the subtropical front was not attributed to the Ekman convergence forcing during the occurrence of the ECKB.

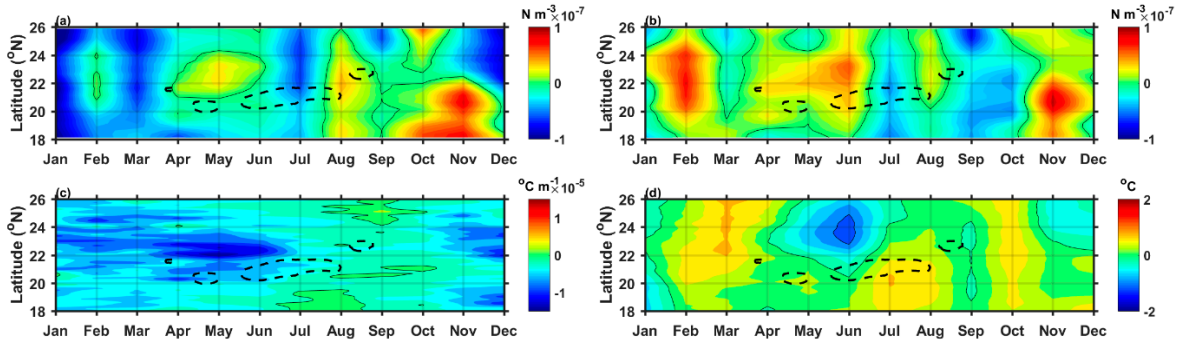

Figure 10. Hovmöller diagram of (**a**) surface wind stress curl, (**b**) surface wind stress curl anomalies, (**c**) meridional gradient of SST, and (**d**) SST anomalies, calculated from the monthly meridional profiles zonally averaged within 125° and 135°E, based on the CCMP wind and OISST data gridded at 1/4° and 0.05° resolution, respectively. Thin solid curves show zero contours. Dashed curves show the contour of zonal geostrophic-current velocity at 0.2 m s^{-1}. The monthly anomalies are herein referred to the monthly climatological fields from 1998 to 2018 due to the available CCMP wind data.

4. Discussion and Summary

This study reports an unusual eastward flow that injected fresher and high-Chl-a-concentration waters into the high-salinity, nutrient-poor NPSG during June and July 2010. The eastward flow was inferred to be the eastward cross-shore Kuroshio branch (ECKB) that sequentially (1) circled an anticyclonic eddy accompanied by high-Chl-a concentrations around the eddy edge; (2) meanderingly flowed eastward with a high Chl-a by following the thermal wind relation; and (3) injected the high-salinity NPSG with fresh waters in which TS properties were similar to those from the KC.

Observed via the satellite ocean-color images, the ECKB appeared as a filament of high-Chl-a concentrations, which were significantly higher than the climatological mean. A drifter trajectory showed that the KC bifurcated near 22°N to the east in May, and flowed eastward with a meandering pattern that matched with the spatial distribution of geostrophic flow and high-Chl-a concentrations in June and July 2010. Our analysis showed that the eastward flow transported the waters with the TS properties similar to those of the KC; thus, we called it the ECKB.

The ECKB carried warmer and fresher waters eastward into the NPSG. The mean geostrophic/Lagrangian speed of the ECKB was approximately 0.5 m s^{-1}, estimated via satellite altimeters, a drifter, and the JMA's 137°E transect. Based on the geostrophic speed at 0.2 m s^{-1}, the ECKB depth approached 200 m, just above the southern boundary of low PV waters (probably the low-PV STMW). The ECKB mechanism was found to be the same as that of the STCC, attributing to a cyclonic wind anomaly to the north at approximately 22–24°N. The cyclonic wind anomaly decreased SST beneath it via Ekman suction and then enhanced the SST front to its south at approximately 21°N. The enhanced SST front subsequently induced the ECKB that was bifurcated from the main stream of the northward-flowing KC.

The injection of warm, fresh, and high-Chl-a-concentration waters into oligotrophic gyres by the ECKB is important to the NPSG ecosystem but it is a largely unexplored issue. Thus, the findings from this study show that the nutrient-poor NPSG can benefit from the KC bifurcation in terms of injection of high-Chl-a-concentration waters, which could potentially influence the marine food webs in the NPSG. However, more in situ observations, are needed, especially on biogeochemical variables, if we are to better understand the impacts of high-Chl-a-concentration waters on higher trophic levels in the nutrient-poor NPSG. Additionally, this study tried to raise the attention of the oceanographic community that the ECKB could be found in other years, and that studying the ECKB interannual variability is important to further understand the connection between the northward-flowing KC and the eastward-flowing STCC.

Author Contributions: Conceptualization, C.-H.C., W.C. and J.-H.T.; methodology, C.-H.C.; software, C.-H.C. and Y.-C.L.; validation, C.-H.C. and Y.-C.L.; formal analysis, C.-H.C., W.C. and Y.-C.L.; investigation, C.-H.C., W.C. and Y.-C.L.; writing—original draft preparation, C.-H.C.; writing—review, revision, and editing, C.-H.C., W.C. and J.-H.T.; funding acquisition, C.-H.C. and W.C. All authors have read and agreed to the published version of the manuscript.

Funding: This research was funded by the Ministry of Science and Technology of Taiwan (R.O.C.), Grant MOST 109-2611-M-019-013 and MOST 110-2611-M-019-019, and by the Ministry of Higher Education of Malaysia FRSG grant (FRGS/1/2018/WAB09/UM/02/4) and the FIO-UM Joint Centre of Marine Science and Technology.

Institutional Review Board Statement: Not applicable.

Informed Consent Statement: Not applicable.

Data Availability Statement: The data presented in this study are available upon request from the corresponding author.

Acknowledgments: W.C. would like to thank the Ministry of Higher Education of Malaysia FRSG grant (FRGS/1/2018/WAB09/UM/02/4) and the FIO-UM Joint Centre of Marine Science and Technology. C.C.H. would like to acknowledge the financial support from the Ministry of Science and Technology of Taiwan (R.O.C.) grants (MOST 109-2611-M-019-013 and MOST 110-2611-M-019-019). This study was conducted using E.U. Copernicus Marine Service Information: <https://doi.org/10.48670/moi-00100, https://doi.org/10.48670/moi-00168, https://doi.org/10.48670/moi-00148, accessed on 31 January 2022>. We thank NASA OBPG for the MODIS-Aqua Level 2 data, Coriolis Operational Oceanography for providing the Argo and surface drifters data, and Remote Sensing Systems for the wind data. We are grateful to the captains and crews of the R/Vs Ryofu Maru and Keifu Maru, and the JMA for their long-term efforts in executing the 137°E repeated hydrographic transects in the North Pacific.

Conflicts of Interest: The authors declare no conflict of interest.

References

1. Nagai, T.; Saito, H.; Suzuki, K.; Takahashi, M. *Kuroshio Current: Physical, Biogeochemical, and Ecosystem Dynamic*; American Geophysical Union, Wiley: Washington, DC, USA, 2019; pp. 1–336. [CrossRef]
2. Chen, C.T.A.; Huang, T.H.; Wu, C.H.; Yang, H.; Guo, X. Variability of the nutrient stream near Kuroshio's origin. *Sci. Rep.* **2021**, *11*, 5080. [CrossRef] [PubMed]
3. Qiu, B. Seasonal eddy field modulation of the North Pacific subtropical countercurrent: TOPEX/Poseidon observations and theory. *J. Phys. Oceanogr.* **1999**, *29*, 2471–2486. [CrossRef]
4. Chu, P.C.; Li, R.; You, X. Northwest Pacific subtropical countercurrent on isopycnal surface in summer. *Geophys. Res. Lett.* **2002**, *29*, 1842. [CrossRef]
5. Qiu, B.; Chen, S. Interannual variability of the North Pacific Subtropical Countercurrent and its associated mesoscale eddy field. *J. Phys. Oceanogr.* **2010**, *40*, 213–225. [CrossRef]
6. Uda, M.; Hasunuma, K. The eastward subtropical countercurrent in the western North Pacific Ocean. *J. Oceanogr. Soc. Japan* **1969**, *25*, 201–210. [CrossRef]
7. Kobashi, F.; Xie, S.-P. Interannual variability of the North Pacific Subtropical Countercurrent: Role of local ocean–atmosphere interaction. *J. Oceanogr.* **2012**, *68*, 113. [CrossRef]
8. Yang, K.-C.; Wang, J.; Lee, C.M.; Ma, B.; Lien, R.-C.; Jan, S.; Yang, Y.J.; Chang, M.-H. Two mechanisms cause dual velocity maxima in the Kuroshio east of Taiwan. *Oceanography* **2015**, *28*, 64–73. [CrossRef]
9. Shih, Y.-Y.; Hung, C.-C.; Gong, G.-C.; Chung, W.C.; Wang, Y.-H.; Lee, I.-H.; Chen, K.-S.; Ho, C.-Y. Enhanced Particulate Organic Carbon Export at Eddy Edges in the Oligotrophic Western North Pacific Ocean. *PLoS ONE* **2015**, *10*, e0131538. [CrossRef]
10. Hsu, P.C.; Lin, C.C.; Huang, S.J.; Ho, C.R. Effects of cold eddy on Kuroshio meander and its surface properties, east of Taiwan. *IEEE J. Sel. Top. Appl. Earth Obs. Remote Sens.* **2016**, *9*, 5055–5063. [CrossRef]
11. Cheng, Y.-H.; Chang, M.-H.; Ko, D.S.; Jan, S.; Andres, M.; Kirincich, A.; Yang, Y.J.; Tai, J.-H. Submesoscale eddy and frontal instabilities in the Kuroshio interacting with a cape south of Taiwan. *J. Geophys. Res. Ocean.* **2020**, *124*, e2020JC016123. [CrossRef]
12. Tseng, Y.-H.; Lu, C.-Y.; Zheng, Q.; Ho, C.-R. Characteristic Analysis of Sea Surface Currents around Taiwan Island from CODAR Observations. *Remote Sens.* **2021**, *13*, 3025. [CrossRef]
13. Chang, Y.; Oey, L. Instability of the North Pacific Subtropical Countercurrent. *J. Phys. Oceanogr.* **2014**, *44*, 818–833. [CrossRef]
14. Yasuda, T.; Hanawa, K. Decadal changes in the mode waters in the midlatitude North Pacific. *J. Phys. Oceanogr.* **1997**, *27*, 858–870. [CrossRef]

15. Kobashi, F.; Mitsudera, H.; Xie, S.-P. Three subtropical fronts in the North Pacific: Observational evidence for mode water-induced subsurface frontogenesis. *J. Geophys. Res.* **2006**, *111*, C09033. [CrossRef]
16. Qiu, B.; Chen, S. Decadal variability in the formation of the North Pacific Subtropical Mode Water: Oceanic versus atmospheric control. *J. Phys. Oceanogr.* **2006**, *36*, 1365–1380. [CrossRef]
17. Sugimoto, S.; Hanawa, K. Impact of Aleutian Low activity on the STMW formation in the Kuroshio recirculation gyre region. Geophys. *Res. Lett.* **2010**, *37*, L03606. [CrossRef]
18. Takeuchi, K. Numerical study of the seasonal variations of the Subtropical Front and the Subtropical Countercurrent. *J. Phys. Oceanogr.* **1986**, *16*, 919–926. [CrossRef]
19. Zhang, Z.; Xue, H. The possible formation mechanism of the Subtropical Countercurrent in the Pacific Ocean. In Proceedings of the EGU General Assembly 2020, Online, 4–8 May 2020. EGU2020-6635. [CrossRef]
20. Talley, L.; Pickard, G.; Emery, W.; Swift, J. *Descriptive Physical Oceanography*, 6th ed.; Elsevier: San Diefo, CA, USA, 2011; pp. 308–311. [CrossRef]
21. Nan, F.; Xue, H.; Yu, F. Kuroshio intrusion into the South China Sea: A review. *Prog. Oceanogr.* **2015**, *137 Pt A*, 314–333. [CrossRef]
22. Trott, C.B.; Metzger, E.J.; Yu, Z. Investigating mesoscale eddy characteristics in the Luzon Strait region using altimetry. *Ocean Dyn.* **2021**, *71*, 679–698. [CrossRef]
23. Saulquin, B.; Gohin, F.; d'Andon, O.F. Interpolated fields of satellite-derived multi-algorithm chlorophyll-a estimates at global and European scales in the frame of the European Copernicus-Marine Environment Monitoring Service. *J. Oper. Oceanogr.* **2019**, *12*, 47–57. [CrossRef]
24. Good, S.; Fiedler, E.; Mao, C.; Martin, M.J.; Maycock, A.; Reid, R.; Roberts-Jones, J.; Searle, T.; Waters, J.; While, J.; et al. The Current Configuration of the OSTIA System for Operational Production of Foundation Sea Surface Temperature and Ice Concentration Analyses. *Remote Sens.* **2020**, *12*, 720. [CrossRef]
25. Oka, E.; Ishii, M.; Nakano, T.; Suga, T.; Kouketsu, S.; Miyamoto, M.; Nakano, H.; Qiu, B.; Sugimoto, S.; Takatani, Y. Fifty years of the 137°E repeat hydrographic section in the western North Pacific Ocean. *J. Oceanogr.* **2018**, *74*, 115–145. [CrossRef]
26. Large, W.G.; Pond, S. Sensible and latent heat flux measurements over the ocean. *J. Phys. Oceanogr.* **1982**, *12*, 464–482. [CrossRef]
27. Pedlosky, J. The dynamics of the oceanic subtropical gyres. *Science* **1990**, *248*, 316–322. [CrossRef] [PubMed]
28. Yan, Y.; Xu, D.; Qi, Y.; Gan, J. Observations of Freshening in the Northwest Pacific Subtropical Gyre near Luzon Strait. *Atmos.-Ocean* **2012**, *50* (Suppl. 1), 92–102. [CrossRef]
29. Xu, L.; Li, P.; Xie, S.-P.; Liu, Q.; Liu, C.; Gao, W. Observing mesoscale eddy effects on mode-water subduction and transport in the North Pacific. *Nat. Commun.* **2016**, *7*, 10505. [CrossRef]